Mapping strain modulated electronic structure perturbations in mixed phase bismuth ferrite thin films

P.S.S.R. Krishnan[a,*,], J.A. Aguiar[b,c,*], Q.M. Ramasse[d], D.M. Kepaptsoglou[d], W.-I. Liang[e], Y.-H. Chu[e], N. D. Browning[f], P. Munroe[a] and V. Nagarajan[a]

[a] School of Materials Science and Engineering, University of New South Wales, Sydney NSW 2052, Australia

[b] Material Science and Technology Division, Los Alamos National Laboratory, Los Alamos, NM 87545, USA

[c] Materials and Characterization, National Renewable Energy Laboratory, Golden, CO 080401, USA

[d] SuperSTEM Laboratory, STFC Daresbury Campus, Keckwick Lane, Daresbury, WA4 4AD, United Kingdom

[e] Department of Materials Science and Engineering, National Chiao Tung University, Hsinchu 30010, Taiwan

[f] Fundamental and Computational Sciences Directorate, Pacific Northwest National Laboratory, 902 Battelle Boulevard, Richland, WA 99352, USA

* Equal contribution

Abstract

Strain engineering of epitaxial ferroelectrics has emerged as a powerful method to tailor the electromechanical response of these materials, although the effect of strain at the atomic scale and the interplay between lattice displacements and electronic structure changes are not yet fully understood. Here, using a combination of scanning transmission electron microscopy (STEM) and density functional theory (DFT), we systematically probe the role of epitaxial strain in mixed phase bismuth ferrite thin films. Electron energy loss O K and Fe $L2,3$ edge spectra acquired across the rhombohedral (R)-tetragonal (T) phase boundary reveal progressive, and systematic changes, in electronic structure going from one phase to the other. The comparison of the acquired spectra, with theoretical simulations using DFT, suggests a breakage in the structural symmetry across the boundary due to the simultaneous presence of increasing epitaxial strain and off- axial symmetry in the T phase. This implies that the imposed epitaxial strain plays a significant role in not only changing the crystal-field geometry, but also the bonding environment surrounding the central iron cation at the interface thus providing new insights and a possible link to understand how the imposed strain could perturb magnetic ordering in the T phase BFO.

Introduction

Strain engineering of epitaxial oxide thin films has evolved into a powerful and innovative method to enhance the functional properties of oxide materials. In ferroelectrics and multiferroics the imposed interfacial strain can enhance polarization, force a heightened sensitivity to electric/magnetic fields and, as recently shown for bismuth ferrite, dramatically improve the electromechanical response.[1] This discovery of a large electromechanical response at the strain-driven morphotropic phase boundary (MPB) in bismuth ferrite (BFO),[1, 2] has initiated an immense research effort directed towards understanding the phase evolution and its correlations with functional properties.[3-6] At the MPB in BFO there coexists highly distorted tetragonal (T) and monoclinic (strained rhombohedral) (R) phases, and hence the material is often termed mixed phase BFO. Further research has shown that the T- and R- phases are related to the monoclinically distorted M_c and M_A phases respectively (thus in the strictest sense these are only T-like and R-like in structure).[3] It was also shown that the monoclinically distorted T-phase relaxes to a complex mixed phase structure with increasing thickness.[7] Nevertheless to be consistent with the original finding by Zeches [1] *et al*., we refer to the highly compressively strained supertetragonal phase as T- and the low-strained rhombohedral-like monoclinically distorted as the R-phase. In the T phase a colossal ferroelectric polarization has recently been observed on account of the measured higher axial (c/a) ratio.[8, 9] X-ray absorption spectroscopy (XAS) studies reveal suppressed magnetic order in the T phase, which is attributed to changes in the bonding environments surrounding the central iron cation.[10] On the other hand, the creation of magnetic moments in highly-strained R ferrite needles has recently also been reported.[11] Whilst the microscopic origins of these changes in polarization,[8] as well as the role of the oxygen octahedral distortions on the phase evolution,[12] are now well understood, investigations of the underlying effect of strain across the MPB on the local atomic electronic structure still remains nascent. Since the electronic and spin properties of multiferroic oxides are intimately linked to the electronic structure of the magnetic

2

cation,[13] a focused study on the electronic structure is critical, especially at the MPB. As the constituent phases of mixed phase BFO are nanoscale in dimensions, such investigations must include experimental and theoretical techniques with single atom and vacancy sensitivity to discern electronic structure lattice correlations within the individual phases and their possible impact on emergent multiferroic properties.

Techniques such as XAS[10, 14] and near-edge X-ray fine absorption spectra (NEXAFS),[15] can typically detect minute spectral changes in the bulk electronic structure. However, these are not well suited to investigate progressive changes in the electronic structure as a function of spatial location across an interface. Scanning transmission electron microscopy (STEM) and STEM-based electron energy loss spectroscopy (EELS)[16] are methods that are able to provide the spatial distribution of electronic phenomena at nanocomposite interfaces with single atom and vacancy sensitivity.[17-20] The unique combination of STEM and density functional theory (DFT) computations further provides valuable insight into the observed electronic structure changes controlling functional responses of these heterostructures.[21-25] Recent work by different groups utilizes this same combination to reveal the role of oxygen and changes to the crystal symmetry in controlling the electronic structure on either side of oxide interfaces.[22, 26-28] In order to address the effect of strain-induced configurations at the mixed phase BFO interface comprising of T and R phases, a study considering the progressive changes across the highly strained interface at the atomic scale remains desired.

Here, we combine aberration-corrected STEM and DFT methods to reveal the strain modulated electronic structure and bonding perturbations at the MPB in mixed phase BFO thin films. In contrast to previous works, we focus on the incremental transitions in the electronic signatures across the boundary layer to explain the concomitant roles of the interfacial electronic structure and strain on the observed multiferroic properties. High angle annular dark field (HAADF) and EELS chemical profiling were utilized to observe the atomic structure. STEM-EELS results indicate clear changes in O *K* and Fe

$L_{2,3}$ edge spectral signatures across the MPB layer. Further analyses, including least squares spectral peak fitting and DFT, allow these observed differences to be attributed to changes in the bonding environment surrounding the central iron cation at the interface. More specifically, DFT analysis suggests a breakage in the structural symmetry across the boundary due to the simultaneous presence of increasing epitaxial strain and off axial symmetry in the T phase within the square-pyramidal oxygen cages that were previously predicted to affect magnetic ordering.[14] The symmetry breaking is confined to within fewer than 20 unit cells from the R-T domain interface.

Experimental methods

Thin film synthesis and STEM sample preparations

Epitaxial thin films were deposited on single crystal commercial $LaAlO_3$ (LAO) using pulsed laser deposition (PLD). A KrF excimer laser (wavelength 248 nm) was employed to ablate a commercial $BiFeO_3$ target at the repetition rate of 10Hz. Before deposition, the chamber was pumped down to a base pressure $\sim 1.5 \times 10^{-6}$ Torr. The deposition was carried at a $700^{\circ}C$ substrate temperature in an oxygen environment. An oxygen partial pressure of 100 mTorr was maintained during deposition. Once the ablation was completed, the samples were cooled down in an oxygen environment of 1 atm at the rate of $15^{\circ}C$ per minute.

Atomic force microscopy and X-ray diffraction

Atomic force microscopy (AFM) was carried out using a JEOL 5400 scanning probe microscope. X-ray diffraction (XRD) and reciprocal space mapping (RSM) were carried out using Pan Analytical MRD capable of scanning $2\theta - \omega$ between 15 to 90 degrees.

STEM-HAADF imaging, STEM-EELS and Geometric Phase Analysis

Cross-sectional electron transparent samples were prepared using conventional tripod polishing with water-free glycol-based lubricants followed by room temperature low

energy low-angle ion beam thinning. Atomic resolution HAADF images and electron energy loss spectra across the MPB were obtained on the aberration corrected Nion UltraSTEM 100 at the SuperSTEM facility in Daresbury. The microscope was operated in STEM mode at 100 kV, with a cold field emission gun (FEG) and equipped with a Gatan Enfina spectrometer, able to form ~0.09 nm probes with a 0.30 eV native energy resolution (based on the full-width half maximum of the zero-loss peak, as measured through a small acceptance angle into the spectrometer in optimal conditions). For the spectra presented here, a dispersion of 0.3 eV/channel was used in order to capture simultaneously the O K and Fe $L_{2,3}$ edges, resulting in an effective energy resolution of 0.75 eV, limited by the detector point spread function. The convergence and collection half angles were 31 and 34 mrad, respectively. Particular attention was paid to minimizing the effects of electron irradiation on the sample materials, to assure all the reported results are not attributed to electron-beam damage. The estimated thickness of the TEM sample is ~45 nm based on the integration of zero loss and plasmon peaks. The BFO film thickness is ~ 50 nm based on the low resolution STEM-HAADF image (data not shown). Geometric Phase Analysis (GPA) was performed to resolve the strain distribution across the R-T phase boundary using the FRWR tool Digital Micrograph plug-in.[29] As a first step selected spots from the power spectrum of the STEM-HAADF image were masked to achieve a spatial resolution of 0.8 nm. A cosine smoothening was then applied to further refine the image. The unstrained reference from the LAO substrate is not available due to the restricted field of view in the STEM-HAADF image. Hence, a relatively flat region from the R-phase BFO was selected as internal reference. A flat region at approximately 1 to 2 nm from the R-T interface towards the R-phase (lower right hand side of STEM-HAADF) was chosen as an internal reference. All the strain values reported here are with reference to this internal reference. The directional co-ordinates referred in the strain mapping are not indicative of the parent crystallographic direction. They are indication of strain tensor of a particular feature in the image. We predict that given the MPB nature of the interface, such possibility is expected.

Model calculations

We employed the full potential (linearized) augmented plane wave plus the local orbital (LAPW+lo) method as implemented in the latest version of the WIEN2K code. Ground state calculations were performed using both the Perdew, Burke, and Erzenhof (PBE)[30] version of the Generalized Gradient Approximation (GGA) plus an effective Hubbard U (2 eV)[31] term on the Fe d states and screened PBE hybrid approach assuming relaxed primitive geometry, using the experimental values for the lattice constants as an initial start to relax the structure, with supercells of size (3 x 3 x 3), in order to enable an investigation of the displacement of the Fe cation. For each computation, 26 and 32 irreducible k-points were employed for the T and R phases respectively. The basis set cutoff parameters were G_{max} = 12 and $R_{mt} \cdot K_{max}$ = 9 (R_{mt} is the smallest atomic sphere radius in the unit cell and K_{max} is the magnitude of the largest k vector) with muffin-tin radii of 1.98 Bohr atomic unit (a.u.) for Bi, 1.77 a.u. for Fe, and 1.57 a.u. for O in the T phase and 2.39 a.u. for Bi, 1.89 a.u. for Fe, and 1.44 a.u. for O in the R phase. The core hole effect [32] was not included since the difference with ground state was small and thereby a comparison to ground state calculations remains useful. Crystal structures were built and results were visualized using CrystalMaker and Vesta.

Spectral creation and peak analysis

To compute the oxygen K edge ELNES profile, WIEN2k's[33, 34] module TELNES3 was used. The TELNES module calculates the double differential scattering cross-section (DDSCS) by performing an iterative summation over all occupied initial and empty states as described in Shirley and Jorissen.[35, 36] The oxygen K edge, with an onset energy of 530 eV, was calculated over an energy grid ranging from -5 to 35 eV with 0.01 eV dispersion using a 100 kV beam with a probe convergence and collections half angles of 31 and 34 mrad respectively. In each case, a summation over scattering angle was then performed and finally a Gaussian smearing is applied to mimic a lifetime broadening and an

instrumental probe broadening where individual spectral profiles varying in broadening from 0.1 to 1.0 eV were calculated to achieve the best qualitative and quantitative fit with experimental spectra. The STEM-EELS linescan direction and probe profile specifics based on the reported aberration values were furthermore considered in calculating the probed oxygen columns throughout the entire sample thickness. The correlation between the computed theoretical and experimentally acquired spectra is based on peak fitting. Each spectrum (experimental or simulated) is decomposed into a series of peaks, whose relative positions and subtended areas can be compared. The positions of the peaks were determined by using multiple linear least squares (MLLS) fitting comprised of Gaussians. Gaussian peaks were fit to lowest standard deviation based on an initialized standard set of Gaussian peak positions, intensities, and peak widths. By applying MLLS peak fitting for each acquired spectrum in the experimental linescan with an initial standard set of guesses for the variables, we are able to resolve relative trends in peak positions and intensities as a function of the linescan position. This analysis was robustly applied to attain the best fit with the data, within a 95% confidence interval. The positions and intensities of those peaks where finally tabulated and compared to investigate trends in the spectral character for both the collected the O K- and Fe $L_{2,}$- edge spectra.

Results and Discussion

Structural characterization

Figure 1(a) is a θ-2θ XRD plot that confirms the presence of a phase-pure BFO film grown epitaxially along the (001) direction on the LAO substrate, consisting of both the T and R phases. The lattice parameter along c-axis of the T-phase was measured to be 0.464 nm and the c-axis of the strained R-phase to be 0.397 nm. Figure 1(b) is the corresponding AFM image of the film that reveals a striated topography, a characteristic

surface feature found for mixed phase BFO. Figure 1(c) is a high resolution STEM-HAADF image of the investigated R-T interface acquired along [001] zone axis orientation. Fourier Transforms (FFT), shown as inserts, also confirm the co-existence of both R and T phases. There is also a broad, low-intensity peak, with an approximate center at ~41.8 degrees. Critically, despite a significant difference in the c/a ratio (~ 1.23 %)[9] between the two phases, both coherently coexist at the interface without the need to form any structural defects. This low-intensity diffraction peak hints at the presence of an interfacial region with continuously varying strain in order to continuously relax from the T-phase to the R-phase. The fact that the peak is low-intensity and broad in nature means it stems from a phase that is either low in volume, or has progressive changes in lattice parameter, which would lead to significant peak broadening. Further, the AFM image reveals no such presence secondary phase crystallite. Given that our high resolution STEM images do not reveal any secondary phases or short-range ordering, this broad low intensity peak may very well represent diffraction from the interfacial transitional regions wherein the large out-of- plane strain is gradually relaxed from the T to R phase. The presence of an interfacial transition region was indeed discussed theoretically by Hatt[31] *et al.,* and forms the major focus of the latter part of this report.

A Geometric Phase Analysis (GPA) of the R-T interface is shown in figures 1(d)-1(f) respectively for E_{xx}, E_{yy} and E_{xy} components of the strain tensor. The E_{xx} component of the strain tensor (perpendicular to the interface) shows a clear distribution of strain variation between the R-T phases of the BFO. The strain component along the interface E_{yy} varies at a much lower level. The calculated misfit strain for R–phase BFO is ~ -0.17%, compares well with the GPA ~-0.2%. Similarly the T phase calculated misfit values at ~+0.14 matches well the GPA ~+0.18%. Thus, the strain mapping clearly confirms the expected lattice distortion between the R and T phases. Further, the GPA mapping is also in agreement with the previous report by Rossell *et al.*, where they reported the misfit strain between R and T phases is predominantly in the out-of-plane direction.[28]
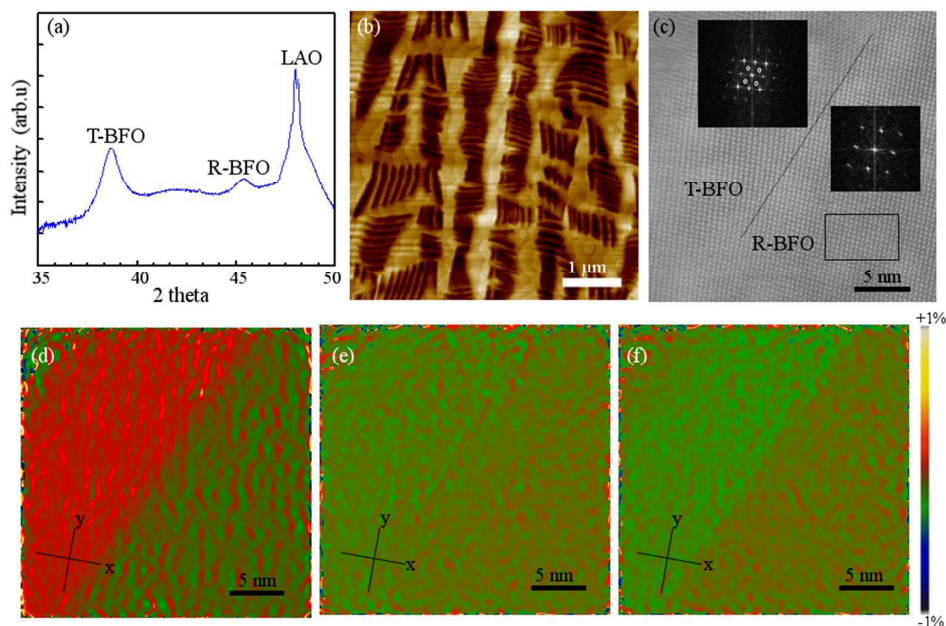
Fig.1 (a) XRD image confirming the presence of T and R phase BFO, (b) AFM image showing the topography of mixed phase BFO, (c) High resolution STEM-HAADF image of the R-T interface with the film in [001] zone axis orientation. The FFT insets confirm the co-existence of R-T phases. The small white circle indicates the extra diffraction spot for the T-phase. (d-f) Geometric phase analysis of image (c) showing the clear distribution of strain in the R and T phase BFO. The strain tensors Exx, Eyy, and Exy are shown as (d), (e) and (f) respectively. A flat region, approximately 1 to 2 nm from the R-T interface towards the R-phase, was selected as an internal reference and this is indicated by the black rectangular box in Fig.1 (c). The directional co-ordinates are same as shown in Fig.2(a).

Electronic structure analysis using experimental O _K_ EEL spectra

In order to understand the electronic structure across the R-T phase boundary, we acquired a number of STEM-EELS linescans by moving the electron probe serially across the R-T phase boundary. An electron energy loss spectrum was recorded at each point. An example of this is shown in Figure 2(a), where the white line indicates the path of the line scan and individual circles being the location where some representative EEL spectra

were acquired. It goes from the R-phase point 1, brown circle) to T-phase (point 10, black circle). Since the focus of this study is the electronic structure and the concomitant role of atomic structure in driving ferroelectric properties, we probed the Fe-O bond by acquiring both the O K (531 eV) and Fe $L_{2,3}$ (710 eV) core loss edges. The scan direction was from the R phase (point 1, brown circle) to the T phase (point 10, black circle) along the [110] unit cell direction.
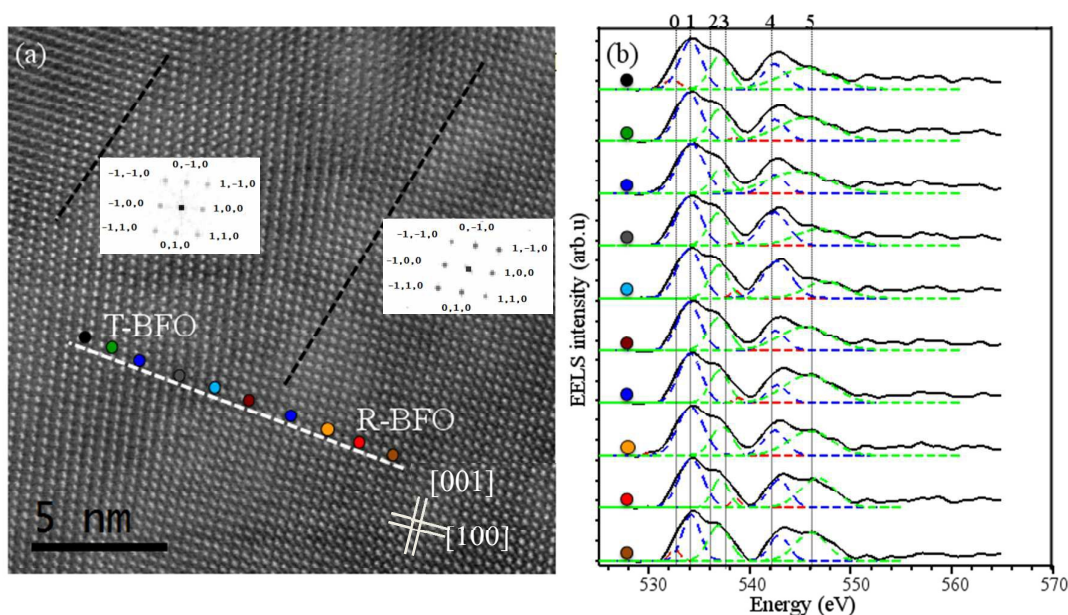
Fig.2 (a) Spectrum image of the R-T interface showing the region (white line) where the EELS scan was carried out. The directional co-ordinates are given as insert. (b) O K EEL spectra across the R-T interface, the experimental spectra is given by the solid black line, while the simulated spectra is shown as dotted color lines. Dotted vertical lines indicate the peak positions and their respective changes across the R-T interface.

The solid black lines in Figure 2(b) are the acquired STEM-EELS O *K* edge spectra for each location indicated on the white line, where subtle spectral changes are observed throughout the linescan across the R and T phases. These spectra typically consist of three low energy features, henceforth the labelled peaks 0 (532 eV), 1 (534 eV), 2 (537 eV). No major change is observed in these three lower energy peaks. A broad hump-like feature, marked as peak 3, is observed at 538.5 eV in both the R- and T-phases. Following the first primary peak, two broad high-energy peaks labeled 4 (543 eV) and 5 (546 eV) span the 540 to 550 eV energy range. These two broad peaks clearly inversely differ between the R- and T-phases.

For *ABO₃*-type perovskites the shape and intensity of the O *K* edge EEL spectrum can reveal minute structural and chemical changes.[22, 37-39] In iron oxide systems, the O *K* edge typically consists of a low energy feature at the edge onset at 531 eV, which is a direct measure of iron's valence state, whereas the higher energy loss peaks provide information regarding the Fe-O bonds.[40, 41] Given the sensitivity of the O *K* edge to minute changes in lattice dimensions and surrounding electronic structure, we argue that the observed fine structure changes are likely related, at least in part, to the effect of strain on Fe-O bond lengths

Electronic structure analysis using DFT O *K* EEL spectra

In order to quantitatively assess the subtle changes in position, intensity, and width of these peaks, a least squares peak fitting procedure was carried out using Gaussian functions to model each of the aforementioned peaks: see Aguiar *et al.*,[42] for further details on the procedure. The colored dotted lines in Figure 2(b), shows these fitting results, for a number of representative points across the entire linescan. The most striking spectral changes concern the edge onset (peak 0), which shifts to lower energy loss by ~ 1 eV when moving from the R to the T phase, and the fine structure associated with the secondary peak (peaks 4-5). The clearly observed shift in the edge onset of

11

peak 0 can be indicative of a change in iron valence between the two phases.[43] Similarly, both peaks 4 and 5 shift to higher energy loss by approximately 1 eV. Additionally, whereas peak 4 shows a near constant intensity on either side of the interface, peak 5 is much weaker (and broader) in the T phase. Further details on changes in the peak position and peak intensity across the R-T interface are given separately in the supplementary section, S1.

The clear behaviour associated with the fourth and fifth peaks is consistent with the previous XAS findings of Ko *et al.*, who concluded the distinct levels of orbital anisotropy going from the T to the R phase effectively perturb the next nearest neighbour atomic configuration.[10] Electronic transitions to the hybridized O 2*p* and Fe 4*sp* states are therefore directly affected. This is also in line with the findings of Ryu *et al.*,[14] who showed very clearly that epitaxial strain had a profound influence on the degree of orbital overlapping, as well as the Fe-O-Fe bond angle. As noted by Saeterli *et al.,*[44] covalent bonding between the *O* p and *Bi* p states also contributes to the secondary peak.

In order to fully understand this transition from the T phase to the R phase one needs to account for the subtle changes in the electronic environments as the electron beam traverses the boundary. For this purpose we resort to DFT modelling. We begin by setting up an idealized atomic-scale interface model in Figure 3 based on the STEM images. Figures 3(a) and 3(b) show the atomic arrangements for the T and R phases, respectively. The in-plane lattice parameter 0.375 nm and out-of-plane lattice parameter 0.465 nm were considered respectively for T-phase BFO.[8] For the R phase a pseudo-cubic lattice parameter for 0.396 nm and α = 59.35 to 60^0 were considered.[45] We assume initially that neither phase has any residual epitaxial strain, although this restriction is later removed. All unit cells used in our simulations use structural parameters either given by Hatt *et al.*,[31] or earlier work of Rossell *et al.*[7,28] In addition to these well-established BFO phases, we also considered the transitional interface

structures (Figure 3c) predicted by Hatt *et al.*[31] These transitional structures are composed of the R-like *Cc* phase (we call this the R' phase) and T-like *Cc phase* (termed here as T'), which result in a predicted transitional path of R (R3c)→R' (Cc)→T'(Cc)→T(P4mm).
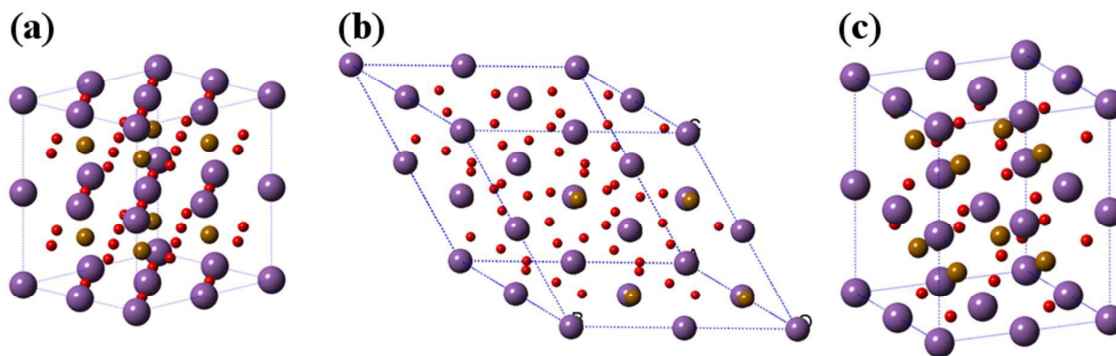
Fig.3 (a), (b) and (c) Schematic of T-phase, R-phase and interface unit cells considered for DFT modelling respectively. The lavender balls represent Bi, brown represent Fe and red represent oxygen.

A series of theoretical O *K* edge spectra were then calculated for the T and R phases, including the effects of additional structural perturbation (discussed below) as well as transitional phases (T' and R') (see the experimental methods section for further details).[31] We note at this point that within DFT there is a limitation on calculating the exact state occupancies. So while DFT does calculate the relative peak positions within decent agreement with experiment, the experimental intensities of the peaks are often not fully reproduced by these models. Progressive trends in the spectra nevertheless are captured providing a particularly useful tool to assess the origin of spectral features.

We begin by examining the effect of epitaxial strain on the O *K* spectral features for the T and R phase. Figures 4(a) and 4(b) show the predicted spectral changes due to the effect of an in-plane compressive strain applied to the reference T phase and R phase respectively. The calculated series is restricted to a limited range of structural distortions

with c/a being varied from 1.20 to 1.28 for the T-phase and 0.96 to 1.10 for the R phase. In the T phase, there are two non-equivalent oxygen positions. Calculations were carried out independently for both positions. We note that the conditions used here do not allow us to distinguish experimentally between these non-equivalent positions. In fact, the observed spectra, arise from a mixed contribution from both types of O columns.[46] Both types of calculated spectra are remarkably alike and show very similar behaviour when varying epitaxial strain. Hence, they can be discussed together, while for simplicity an average of the two positions is shown on Figure 4(a). Six characteristic peaks, denoted as peak 0 to peak 5 are observed. Low energy peaks 0 and 1 show a very subtle variation (approximately merging into a single peak) as the strain is increased gradually, while peak 2 remains constant at all the c/a ratios. There is no change observed for the higher energy peaks (3, 4 and 5). We thus suggest that applying strain (along the c-axis) alone is not enough to perturb the next nearest neighbour atomic configurations (which were found to give rise to the changes in peak 5 experimentally by Ko *et al.*).[10]

On the other hand, in the R phase, (Figure 4(b)), for which there is only one type of O position, the low energy peak 2 shifts towards lower energy by ~ 1 eV, while all the other peaks (1,3 and 4) remain the same as the c/a is gradually increased from 0.96 to 1.10. Most critically, we show that the peak at 0 position is either absent (or distinctly weak). As this low energy peak typically signifies a direct measure of the local valence state for the central iron cation, it presumably hints that the local electronic structure for Fe has begun to vary. As stated earlier, in the Fe-O system, the EELS signature primarily consists of a) a low-energy region (~530 eV) which is characteristic of the Fe valence state and b) a high-energy region (~545 eV) which is characteristic of the extended surrounding Fe-O bonding environment. Based on our present DFT calculations, it can be stated that in both the T and R phase, a subtle variation possibly affecting the Fe valence is observed under strain, while it appears that the Fe-O bonding is relatively insensitive to the applied strain in both the phases.
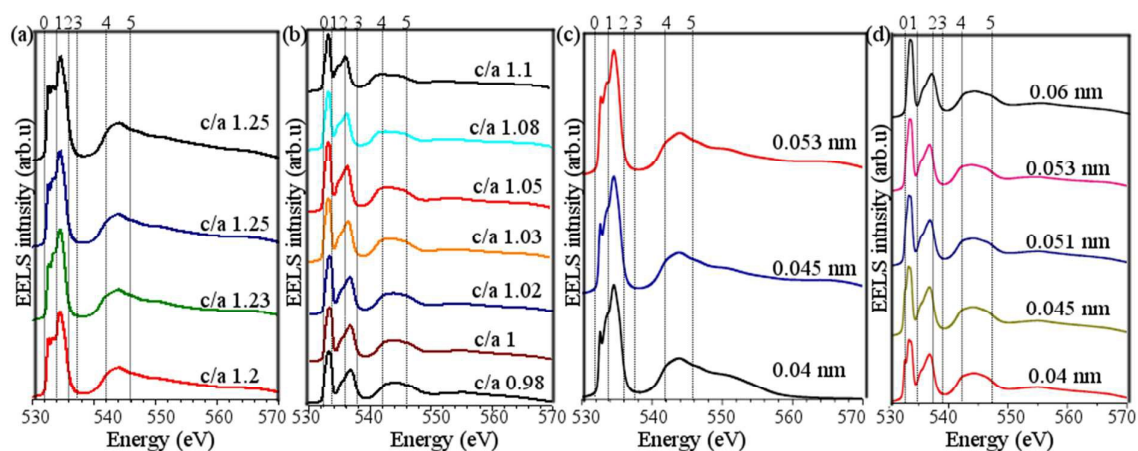
Fig.4 (a) The DFT based simulated O *K* EEL spectra for varied epitaxial strain (c/a varying from 1.2 to 1.28) for T-phase BFO, (b) the R-phase BFO O *K* simulated EEL spectra for different c/a (0.98 to 1.1), (c) and (d) the simulated O *K* EEL spectra for the T and R phase respectively for varied Fe cation displacement values. In all images spectral positions are marked with black dotted line for easy viewing.

In addition to the influence of strain on the EELS fine structure, we also considered the effect of off-axial central displacement of the iron cation relative to the surrounding oxygen anions for a series of c/a axial ratios. These results are shown in Figure 4(c) and 4(d) for the T and R phases, respectively. The values of cation displacements chosen correspond to those experimentally found by Rossell *et al.*,[28] and Lubk *et al.*[45] From Figure 4(c) it can be observed that cation displacements do not noticeably affect the O *K* edge fine structure in the T phase. In contrast Figure 4(d) shows that the pre-peak (numbered as 0) becomes less pronounced as the cation displacement distance is increased, although the higher energy peaks show no such variation. Therefore increasing the cation displacement in the R phase may result in a subtle change in Fe valence, which does not occur in the T phase.

We next examine the O *K* edges calculated by DFT for the two interfacial T' and R' phases, shown in Figures 5(a) and 5(b) respectively. For the purposes of brevity, we

focus here on results for a fixed c/a axial ratio (*i.e.* a given level of strain) of 1.23 since it corresponds to the structure predicted by Hatt *et al.*[31] We also note that the off-axial displacement of the central iron cation (given in [31]) relative to the surrounding oxygen anions is markedly distinct from the pure T and R phases. As suggested by Stokes *et al.* this distortion lowers the crystal symmetry into a polar space group,[47] resulting in effectively the same perturbations as in the transitional tetragonal Mc phase and rhombohedral Ma phase.[48] In these structures, the oxygen positions are thereby no longer equivalent and in order to capture the effects of the distortion on the EELS spectrum, we must again compute each distinct atomic oxygen spectrum. As per the theory the five-fold symmetry for the T' phase results in 5 non-equivalent oxygen spectra and 4 non-equivalent spectra for the R' phase, shown in Figure 5(a) and (b) as colored lines and labelled accordingly. However, due to experimental limitations the observed spectra will arise in practice from a combination of contributions from the different O sites. Therefore, for the DFT computations to be as realistic as possible and their comparison to the experimental data to be meaningful, a (weighted) average spectrum should be created from these 5 (or 4) constituents, ideally also taking into account the crystallographic direction because of the role of crystallographic anisotropy and channeling on the shape of the O *K* edge.[49] This average spectrum is shown as the solid black line.

The following observations are made:

(a) for the T' phase the pre-peak (0) intensity exhibits a broad shoulder, whilst for the R' phase this peak is much sharper and more distinct. (b) in the same vein, peaks 1 and 2, computed by DFT for the T' phase, are also less sharp than the corresponding peaks for the R' phase. As previously mentioned[44] peaks 1 and 2 indicate the strength of the hybridization between the O and Bi ions and hence indicate how Bi-O bond length changes affect the extended fine structure. It is not surprising that the larger Bi-O bond length in the T' derivative compared to the R' derivative would result in a weaker Bi-O

16

hybridization. (c) The strength of peak 3 increases comparing the T' with the R', whilst peaks 4 and 5 are much weaker in the T' phase in comparison to the R'. Again, this would mean that the nearest neighbour interactions in the R' phase have a stronger influence on the Fe-O bonding environment compared to the T' phase.
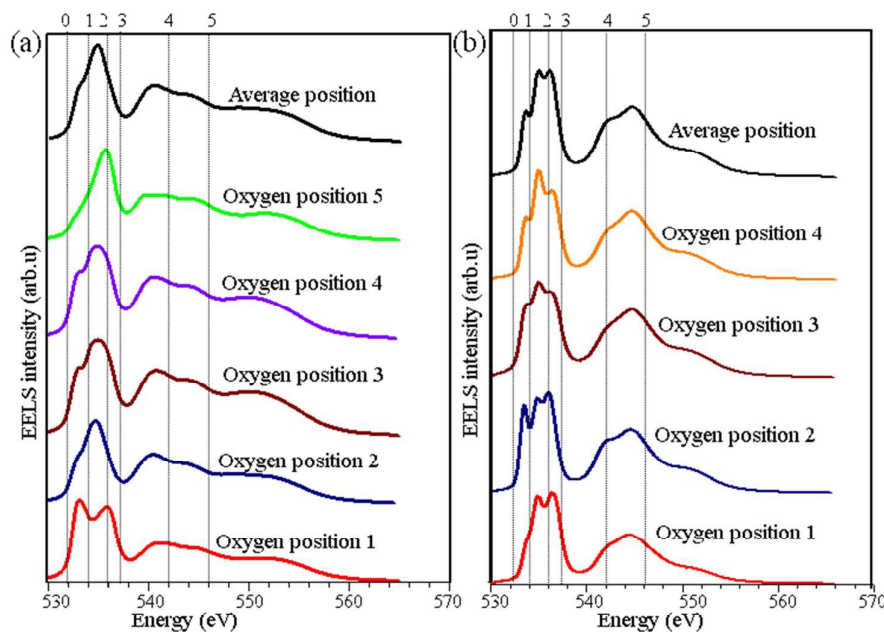
Fig.5 (a) Simulated O K spectra for the intermediate T'-like BFO phase with fixed c/a 1.23 and (b) Simulated O K spectra for the R'-like BFO phase for a fixed c/a 1.23. In all images spectral positions are marked with black dotted lines for easy viewing.

It is clear from these DFT results that no single effect, be it pure strain, cation displacement or even shear (due to stoichiometry and matching interface polarity the model must include a shear tilt if the transitional structure is to be considered- the effect of shear is discussed in supplementary S2), can fully explain the observed experimental changes. Some of the individual trends are well reproduced however, such as the relative intensity variations and shifts in peaks 4 and 5 in the T phase. An instructive

attempt at a point-by-point fit of the experimental linescan to the library of calculated spectra was thus made. Although obtaining a direct one to one match is highly unrealistic, the approach nevertheless establishes a direct correlation between DFT, electronic modifications, and EELS in order to build a simplistic picture of the structural evolution at the MPB.

The modified statistical approach of Aguiar *et al.,* was used to determine the closest match between experimental and calculated spectra.[42] To keep the computations tractable, only the strain and displacements were varied for the entire ranges considered (as given in figure 4). The shear series was calculated for fixed strain and displacement values. This procedure, described in greater detail elsewhere (see supplementary S3), relies on a least-squares optimization to compare the intensities and positions of individual peaks (all modelled by Gaussian functions) of all spectra.

The results of this fitting procedure are shown in Figure 6. (see supplementary S3 for fitting parameters). In each case a heavy dashed line represents the best fit. We note that the fitting procedure was done in a "blind" fashion. That is, no *a priori* knowledge was assumed and for each spectrum each of the above parameters was varied across the entire range. Following this a best-fit candidate was chosen. The best match to the spectra identified by brown, red and yellow coloured small circles in Figure 6 is obtained with theoretical spectra calculated from R-phase BFO. This is reassuring as indeed this region corresponds to the R-phase. On the other hand, for the spectra identified as blue, dark red and purple small circles, in the vicinity of the interface, the best fit is only found when using a transitional T' phase model with c/a=1.18 and a smaller Fe cation displacement taken from the model of Hatt *et al.* The statistical EELS analysis thus appears to confirm experimentally the presence of this intermediate structure at the MPB, over a spatial extent of less than 1 nm. Finally, from that point onward, (spectra identified by a grey small circle and above), the observations are consistent with a

relatively relaxed T phase with a c/a=1.28, which is consistent with the progressive effects of octahedral tilting and Fe-O bond elongation reported by other groups.[22, 28]

However, the simulations show that even taking into account each of the aforementioned factors cannot faithfully reproduce the trends shown for peaks 2 and 3, in particular when we move to the top section of figure 6 (i.e. the T phase). Nevertheless, the behavior of the extended near peaks 4 and 5 is well reproduced. These spectral features are where the most obvious changes occur within the experimental dataset, and, crucially, such higher loss fine features typically act as fingerprint for bond linearity and extended structure geometry (2nd and beyond nearest neighbours). Importantly, the suppression of peak 5 in the T phase coming from the R phase (arguably the most striking difference in fine structure between the two phases) is correctly identified by our EELS analysis. The intensity of this peak is linked to the nearest neighbor distances from the Fe cation. This is smaller in the R phase compared to the T phase. Reproducing faithfully the observed trends here, even if the earlier fine features are less well-reproduced, therefore comforts us in our conclusion that we are obtaining real insights into the structural transition at the boundary.
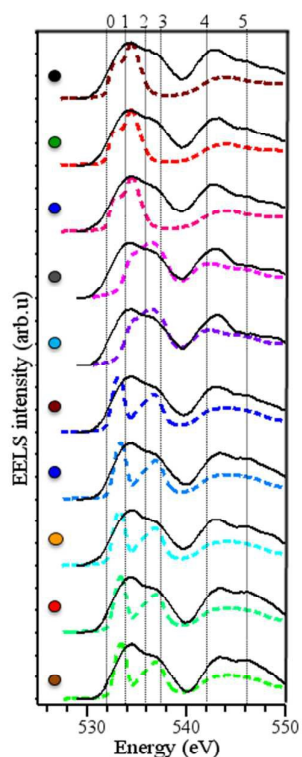
Fig.6 O *K* EEL spectra across the R-T interface matched to experimental data using the modified statistical approach. Best fit is achieved for transitional T' phase BFO over a length scale of ~ 1nm (spectra between blue, dark red and lavender colors), while at other regions the simulation matches with individual R (green color) and T (red color) phases.

Electronic structure analysis using experimental Fe $L_{2,3}$ EEL spectra

The magnetic behaviour of BFO is due in large part to the significant displacement of the central Fe cation with respect to the surrounding octahedral shell, which is expected to influence the crystal-field splitting of 3*d* orbital energy levels. The work of Ryu *et al.,*[14] already confirmed the intimate interdependency between epitaxial strain and the electronic structure of the Fe-O bond, and thus magnetism in strained single-phase BFO epitaxial thin films. The careful comparison of theoretical and experimental O *K* spectra presented above seems to confirm this, and the analysis hints at the presence around

20

the MPB of a small region where BFO conforms to a transitional T' phase, for which the Fe cation is displaced by up to 0.1 Å (0.01 nm). We therefore turn our attention to the sensitive Fe $L_{2,3}$ spectral lines, which originate from transitions between the spin-orbit split levels Fe $2p^{3/2}$ and Fe $2p^{1/2}$ ($2p^6 3d^5$) to empty Fe $3d$-states ($2p^6 3d^6$) above the Fermi level.[50, 51] Fe $L_{2,3}$ core loss spectra are known to vary with the oxidation state for the Fe^{x+} cation.[52] A thorough analysis of the Fe $L_{2,3}$ core loss spectra therefore needs be performed to accurately account for the possible changes in electronic structure: indeed, sets of iron-containing standards including ferromagnetic Fe_3O_4, (3+ and 2+) and γ-Fe_2O_3, (3+ and 2+) [15] or anti-ferromagnetic α-Fe_2O_3, (3+) [53] all have well-documented and very distinct Fe $L_{2,3}$ fine structure to which our experimental data can be compared and form a basis for our detailed spectral analysis.

The experimental Fe-$L_{2,3}$ EEL spectra are shown in Figure 7(a) as solid red lines. The Fe $L_{2,3}$ spectra is characterized by three distinct peaks marked as 0, 1 and 2. A pre-peak 0, appearing at ~ 704 eV, forming a part of the L_3 peak and known as the L_{3a} peak, is very distinctly observed up to the dark red spectrum which essentially corresponds to the R phase. On further moving into the T phase, this feature disappears. The characteristic main component of the Fe L_3 peak, labeled here as peak 1 known as the L_3b peak, appears at ~ 707 eV and its intensity is constant in both T and R phases. Peak 2 shows a broad diffuse feature in both phases. The associated peak splitting of the L_3 peak and the presence of a stronger peak 0 in the R phase is a direct consequence of octahedral crystal field splitting of the Fe 3d states into the t_{2g} and e_g levels.
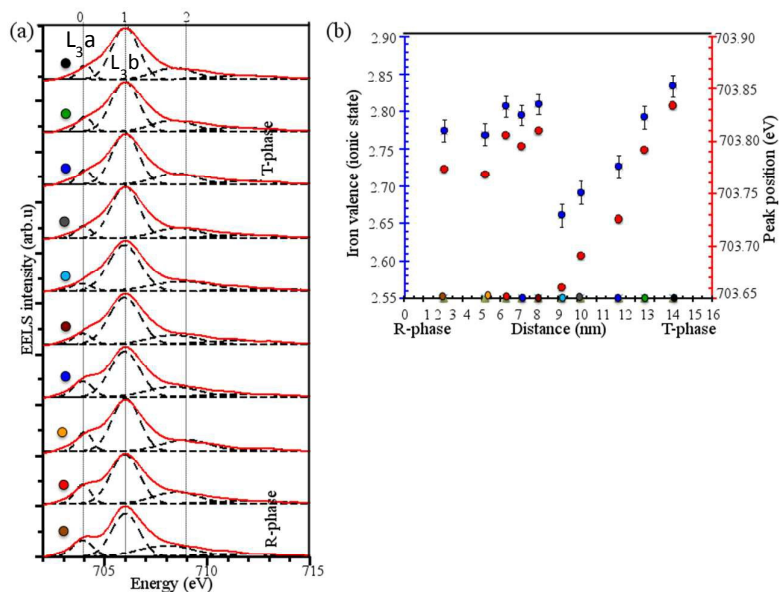
Fig.7 (a) Experimental EEL spectra for Fe $L_{2,3}$ across R-T interface represented by red solid line and simulated EEL spectra represented by dotted black line. The peaks are marked as 0 to 2 and represented using vertical black dotted lines for easy viewing, with the L_3a and L_3b peaks respectively labeled as peaks 0 and 1. (b) The estimated Fe valence change across the R-T interface calculated based on peak fitting of the L_3 EEL peak (details in S4).

Electronic structure analysis using simulated Fe $L_{2,3}$ EEL spectra

The experimental EELS Fe $L_{2,3}$ spectra were analyzed using MLLS peak fitting and fitting results are presented in Figure 7(a) as dotted black lines. Individual Gaussian peaks used for the fit are also referred to by the same peak numbers at their respective energies. Peak fitting clearly confirms the visual inspection of the experimental spectra. The first spectral feature, peak 0, present in the R phase as a shoulder approximately 1.6 eV before the dominant Fe L_3 peak, disappears as the probe moves towards the T phase. This shoulder (peak 0) is typically observed when iron is in Fe^{3+} octahedral coordination, due to the presence of an unpaired electron at the lower energy state (t_{2g}).

The splitting to lower energy loss and the disappearance of this peak are therefore indicators of changes in the atomic binding environment surrounding the Fe cations, and possibly point to a reduction of Fe-O octahedral symmetry [41] going from strained R to a 5-fold symmetry in the strained T phase. As noted elsewhere by Rossell *et al.*,[28] the full crystal field splitting cannot be resolved experimentally along this orientation since in the highly strained T phase one oxygen is displaced to a non-bonding pair, resulting in a change in coordination from an octahedron to a square pyramidal shape with reduced Fe-O bond length. In agreement with their observations, we also cannot clearly observe the splitting in the raw experimental spectra, but the peak fitting procedure clearly demonstrates that these subtle structural changes are still having some effect on the EELS fine structure.

It is possible to estimate quite accurately the Fe oxidation state based either on the L_3 to L_2 intensity ratio[54] or the specific peak shape.[43] In Figure 7(b), the oxidation state of Fe was estimated point by point along the linescan using the latter, where peak fitting of the L_3 peak allowed for a precise description of the peak shape. We note that the integrated L_3 to L_2 intensity method leads to very similar results (not shown here). The L_3 peak spectral character was only assessed after subtracting the decaying background using step profiles spectra.[43, 55, 56] From Figure 7(b), it is observed that the Fe valence is around 2.75 to 2.8 in the R phase, but drops to around 2.6 to 2.7 at the interface region and reaches a value of 2.8 in the T phase for both methods. The L_3/L_2 intensity ratio is shown as blue square markers, while the peak position results are shown as red circle markers. This valence 'map' therefore qualitatively confirms the above discussion, with a clear drop in valence state around the transition area. We note, however, that far from the boundary layer and away from the nanodomains, the iron oxidation state would be expected to nearly reach a 3^+ cation configuration: clearly this is not achieved, which is very likely due to the nanometer size of the various domains. In the region observed, the proximity between domains means no single R or T nano-phase can reach a near-bulk state (see supplementary material S4).

We are now in a position to understand the systematic changes due to the imposed epitaxial strain across the R-T boundary. The interfacial electronic structure is not only affected by a change in iron valence, but also the bond distance changes with neighbouring atoms, as revealed by the concurrent analyses of O K edge and Fe $L_{2,3}$ edge spectra. Across the boundary and into the T phase, the applied strain has a significant effect on the coordination geometry, leading to an increasing degree of square-pyramidal (5-fold) coordination in place of octahedral coordination. Other structural effects such, as displacement of central cation or unit cell shear, were also found to bear on the spectral trends observed for the experimental O K edge, especially with regards to the elongation of the Fe-O octahedron in the T phase. By contrast, the R phase shares no similar shift of Fe-O octahedra and therefore the 3d orbital splitting is nearly resolved. Nevertheless, there still exists residual epitaxial strain, which induces a monoclinic symmetry and a displacement of the central Fe cation as noted by others.[31] For such a case the energies of the ligand field (e$_g$ and t$_{2g}$) are comparable to traditional perovskites[57] and there is no free electron at the low energy state. The gap between high and low energy levels is very narrow (~0.45 x octahedral split energy).[58] Due to this narrow gap, the higher energy states are filled. Under these same conditions, the energy required to displace an electron into a higher orbit is lower than the related pairing energy[59] and, hence, provides additional electrons for creating magnetic moments in agreement with previous XAS and X-ray absorption near edge structure (XANES) analysis of strained single-phase BFO.[14]

Finally, we note that we did not resolve the presence of ordered or confined oxygen vacancies as was shown recently by Borisevich et $al.$[60, 61] for related, although not necessarily identical, samples. Whilst there is ample evidence that oxygen vacancy ordering plays an important role in the functional behaviour of complex oxide thin films, we simply do not see those here. This does not preclude the presence of vacancies as such in our samples. It means currently we do not have evidence how their ordering will influence the observed effects at the R-T interface. Furthermore, the DFT computations

discussed here already take into account a fairly large parameter space. Targeting the influence of vacancies on specific BFO phases forms the part of a future study, where the mean field theory is already in place by some of the co-authors.[62]

Conclusion

A systematic experimental investigation of the structural and electronic structure at the R-T phase phase boundary in (001)-oriented mixed phase BFO films was performed. The goal was to understand the role of perturbation imposed by the epitaxial strain at the phase boundary on the progressive changes in the physical and electronic structure across the phase boundary layer. STEM/EELS linescans performed across the boundary reveal significant and progressive changes in the O K and Fe $L_{2,3}$ edge EEL spectra. Quantitative analysis of the Fe $L_{2,3}$ edge confirms that in the vicinity of the R-T boundary the Fe valence is altered. This can, in turn, be put forward to explain the changes in magnetic behaviour associated with the formation of the T phase thereby revealing the microscopic correlations between the origins of the observed magnetic ordering and the lattice structure. Thus, perturbations in the electronic structure imposed by the epitaxial strain are crucial to the origins of the reported magnetism and multiferroic properties associated with mixed phase BFO.

Acknowledgements

References

1.   R. J. Zeches, M. D. Rossell, J. X. Zhang, A. J. Hatt, Q. He, C.-H. Yang, A. Kumar, C. H. Wang, A. Melville, C. Adamo, G. Sheng, Y.-H. Chu, J. F. Ihlefeld, R. Erni, C. Ederer, V. Gopalan, L. Q. Chen, D. G. Schlom, N. A. Spaldin, L. W. Martin and R. Ramesh, *Science*, 2009, **326**, 977-980.

2.   J. X. Zhang, XiangB, HeQ, SeidelJ, R. J. Zeches, YuP, S. Y. Yang, C. H. Wang, Y. H. Chu, L. W. Martin, A. M. Minor and RameshR, *Nat. Nano.*, 2011, **6**, 98-102.

3.   Z. Chen, Z. Luo, C. Huang, Y. Qi, P. Yang, L. You, C. Hu, T. Wu, J. Wang, C. Gao, T. Sritharan and L. Chen, *Adv. Fun. Mater.*, 2011, **21**, 133-138.

4.   A. R. Damodaran, C.-W. Liang, Q. He, C.-Y. Peng, L. Chang, Y.-H. Chu and L. W. Martin, *Adv. Mater.*, 2011, **23**, 3170-3175.

5.   Z. Chen, L. You, C. Huang, Y. Qi, J. Wang, T. Sritharan and L. Chen, *App. Phys. Lett.*, 2010, **96**, 252903-252903.

6.   A. Kumar, S. Denev, R. J. Zeches, E. Vlahos, N. J. Podraza, A. Melville, D. G. Schlom, R. Ramesh and V. Gopalan, *App. Phys. Lett.*, 2010, **97**, 112903.

7.   A. R. Damodaran, S. Lee, J. Karthik, S. MacLaren and L. W. Martin, *Phys. Rev. B*, 2012, **85**, 024113.

8.   J. X. Zhang, Q. He, M. Trassin, W. Luo, D. Yi, M. D. Rossell, P. Yu, L. You, C. H. Wang, C. Y. Kuo, J. T. Heron, Z. Hu, R. J. Zeches, H. J. Lin, A. Tanaka, C. T. Chen, L. H. Tjeng, Y. H. Chu and R. Ramesh, *Phys. Rev. Lett.*, 2011, **107**, 147602.

9.   H. Béa, B. Dupé, S. Fusil, R. Mattana, E. Jacquet, B. Warot-Fonrose, F. Wilhelm, A. Rogalev, S. Petit, V. Cros, A. Anane, F. Petroff, K. Bouzehouane, G. Geneste, B. Dkhil, S. Lisenkov, I. Ponomareva, L. Bellaiche, M. Bibes and A. Barthélémy, *Phys. Rev. Lett.*, 2009, **102**, 217603.

10.   K.-T. Ko, M. H. Jung, Q. He, J. H. Lee, C. S. Woo, K. Chu, J. Seidel, B.-G. Jeon, Y. S. Oh, K. H. Kim, W.-I. Liang, H.-J. Chen, Y.-H. Chu, Y. H. Jeong, R. Ramesh, J.-H. Park and C.-H. Yang, *Nat. Commun.*, 2011, **2**, 567.

11.   Q. He, Y. H. Chu, J. T. Heron, S. Y. Yang, W. I. Liang, C. Y. Kuo, H. J. Lin, P. Yu, C. W. Liang, R. J. Zeches, W. C. Kuo, J. Y. Juang, C. T. Chen, E. Arenholz, A. Scholl and R. Ramesh, *Nat. Commun.*, 2011, **2**, 225.

12.   B. Dupé, I. C. Infante, G. Geneste, P. E. Janolin, M. Bibes, A. Barthélémy, S. Lisenkov, L. Bellaiche, S. Ravy and B. Dkhil, *Phys. Rev. B*, 2010, **81**, 144128.

13.   R. Ramesh and N. A. Spaldin, *Nat. Mater.*, 2007, **6**, 21-29.

14.   S. Ryu, J.-Y. Kim, Y.-H. Shin, B.-G. Park, J. Y. Son and H. M. Jang, *Chem. Mater.*, 2009, **21**, 5050-5057.

15.   T.-J. Park, S. Sambasivan, D. A. Fischer, W.-S. Yoon, J. A. Misewich and S. S. Wong, *The J. Phys.Chem. C*, 2008, **112**, 10359-10369.

16.   R.F.Egerton, *Electron Energy Loss in the Electron Microscope*, (Plenum press, New York, 1996).

17.   N. Nakagawa, H. Y. Hwang and D. A. Muller, *Nat. Mater.*, 2006, **5**, 204-209.

18.   N. Reyren, S. Thiel, A. D. Caviglia, L. F. Kourkoutis, G. Hammerl, C. Richter, C. W. Schneider, T. Kopp, A.-S. Rüetschi, D. Jaccard, M. Gabay, D. A. Muller, J.-M. Triscone and J. Mannhart, *Science*, 2007, **317**, 1196-1199.

19.   P. Gao, C. T. Nelson, J. R. Jokisaari, S.-H. Baek, C. W. Bark, Y. Zhang, E. Wang, D. G. Schlom, C.-B. Eom and X. Pan, *Nat. Commun.*, 2011, **2**, 591.

20.   D. Muller, *Nat. Materials.*, 2009, **8**, 263-270.

21.   W. Luo, M. Varela, J. Tao, S. J. Pennycook and S. T. Pantelides, *Phys. Rev. B*, 2009, **79**, 052405.

22.   A. Y. Borisevich, H. J. Chang, M. Huijben, M. P. Oxley, S. Okamoto, M. K. Niranjan, J. D. Burton, E. Y. Tsymbal, Y. H. Chu, P. Yu, R. Ramesh, S. V. Kalinin and S. J. Pennycook, *Phys. Rev. Lett.*, 2010, **105**, 087204.

23.   Z. Wang, W. Zeng, L. Gu, M. Saito, S. Tsukimoto and Y. Ikuhara, *J. Appl. Phys*, 2010, **108**, 113701.

24.   L. Bocher, A. Gloter, A. Crassous, V. Garcia, K. March, A. Zobelli, S. Valencia, S. Enouz-Vedrenne, X. Moya, N. D. Marthur, C. Deranlot, S. Fusil, K. Bouzehouane, M. Bibes, A. Barthélémy, C. Colliex and O. Stéphan, *Nano Letters*, 2011, **12**, 376-382.

25.   J. Gazquez, W. Luo, M. P. Oxley, M. Prange, M. A. Torija, M. Sharma, C. Leighton, S. T. Pantelides, S. J. Pennycook and M. Varela, *Nano Letters*, 2011, **11**, 973-976.

26.   H. J. Chang, S. V. Kalinin, A. N. Morozovska, M. Huijben, Y.-H. Chu, P. Yu, R. Ramesh, E. A. Eliseev, G. S. Svechnikov, S. J. Pennycook and A. Y. Borisevich, *Adv. Mater.,* 2011, **23**, 2474-2479.

27.   J. He, A. Borisevich, S. V. Kalinin, S. J. Pennycook and S. T. Pantelides, *Phys. Rev. Lett.*, 2010, **105**, 227203.

28.   M. D. Rossell, R. Erni, M. P. Prange, J. C. Idrobo, W. Luo, R. J. Zeches, S. T. Pantelides and R. Ramesh, *Phys. Rev. Lett.,* 2012, **108**, 047601.

29.   http://elim.physik.uni-ulm.de/?page_id=1044.

30.   J. P. Perdew, K. Burke and M. Ernzerhof, *Phys. Rev. Lett.,* 1996, **77**, 3865-3868.

31.   A. J. Hatt, N. A. Spaldin and C. Ederer, *Phys. Rev. B*, 2010, **81**, 054109.

32.   K. van Benthem, C. Elsässer and M. Rühle, *Ultramicroscopy*, 2003, **96**, 509-522.

33.   C. Hébert, *Micron*, 2007, **38**, 12-28.

34.   K. Schwarz, P. Blaha and G. K. H. Madsen, *Comput. Phys. Commun.,* 2002, **147**, 71-76.

35.   E. L. Shirley, *Phys. Rev. Lett.*, 1998, **80**, 794-797.

36.   K. Jorissen, Ph.D thesis,*University of Antwerp*, 2007.

37.   M. Arredondo, Q. M. Ramasse, M. Weyland, R. Mahjoub, I. Vrejoiu, D. Hesse, N. D. Browning, M. Alexe, P. Munroe and V. Nagarajan, *Adv. Mater.*, 2010, **22**, 2430-2434.

38.   A. B. Shah, Q. M. Ramasse, X. Zhai, J. G. Wen, S. J. May, I. Petrov, A. Bhattacharya, P. Abbamonte, J. N. Eckstein and J.-M. Zuo, *Adv. Mater.*, 2010, **22**, 1156-1160.

39.   A. B. Shah, Q. M. Ramasse, S. J. May, J. Kavich, J. G. Wen, X. Zhai, J. N. Eckstein, J. Freeland, A. Bhattacharya and J. M. Zuo, *Phsy. Rev. B*, 2010, **82**, 115112.

40.   S.-Y. Chen, A. Gloter, A. Zobelli, L. Wang, C.-H. Chen and C. Colliex, *Phys. Rev. B*, 2009, **79**, 104103.

41.   C. Colliex, T. Manoubi and C. Ortiz, *Phys. Rev. B*, 1991, **44**, 11402.

42.   J. A. Aguiar, Q. M. Ramasse, M. Asta and N. D. Browning, *J. Phys. Condens. Mat.*, 2012, **24**, 295503.

43.   P. A. van Aken and B. Liebscher, *Phys. Chem. Miner.*, 2002, **29**, 188-200.

44.   R. Sæterli, S. M. Selbach, P. Ravindran, T. Grande and R. Holmestad, *Phys. Rev. B*, 2010, **82**, 064102.

45.   A. Lubk, M. D. Rossell, J. Seidel, Y. H. Chu, R. Ramesh, M. J. Hÿtch and E. Snoeck, *Nano Letters*, 2013, **13**, 1410-1415.

46.   M. P. Prange, M. P. Oxley, M. Varela, S. J. Pennycook and S. T. Pantelides, *Phys. Rev. Lett.*, 2012, **109**, 246101.

47.   H. T. Stokes, E. H. Kisi, D. M. Hatch and C. J. Howard, *Acta Crystallogr. B*, 2002, **58**, 934-938.

48.   H. M. Christen, J. H. Nam, H. S. Kim, A. J. Hatt and N. A. Spaldin, *Phys. Rev. B*, 2011, **83**, 144107.

49.   M. Bugnet, V. Mauchamp, P. Eklund, M. Jaouen and T. Cabioc'h, *Acta. Mater*, 2013, **61**, 7348-7363.

50. Z. L. Wang, J. S. Yin and Y. D. Jiand, *Micron*, 2000, **31**, 571-580.

51. D. H. Pearson, C. C. Ahn and B. Fultz, *Phys. Rev. B.*, 1993, **47**, 8471.

52. R. D. Leapman and L. A. Grunes, *Phys. Rev. Lett.*, 1980, **45**, 397.

53. J. H. Paterson and O. L. Krivanek, *Ultramicroscopy*, 1990, **32**, 319-325.

54. H. K. Schmid and W. Mader, *Micron*, 2006, **37**, 426-432.

55. P. A. van Aken, B. Liebscher and V. J. Styrsa, *Phys. Chem. Miner.*, 1998, **25**, 323-327.

56. F. Cosandey, D. Su, M. Sina, N. Pereira and G. G. Amatucci, *Micron*, 2012, **43**, 22-29.

57. M. Gu, M. D. Biegalski, H. M. Christen, C. Song, C. R. Dearden, N. D. Browning and Y. Takamura, *J. Mater. Res.*, 2012, **27**, 1436-1444.

58. C. D. Curtis, *Geochim. Cosmochim. Ac.*, 1964, **28**, 389-403.

59. Donald S and McClure, *J. Phys. Chem. Solids.*, 1957, **3**, 311-317.

60. A. Y. Borisevich, Y. Kim, M. P. Oxley, S. J. Pennycook, S. V. Kalinin, A. Morozovska, E. Eliseev, Y. Chu and P. Yu, *Micros. Microanal.*, 2012, **18**, 318-319.

61. Y.-M. Kim, A. Kumar, A. Hatt, A. N. Morozovska, A. Tselev, M. D. Biegalski, I. Ivanov, E. A. Eliseev, S. J. Pennycook, J. M. Rondinelli, S. V. Kalinin and A. Y. Borisevich, *Adv. Mater.*, 2013, **25**, 2497-2504.

62. A. N. Morozovska, E. A. Eliseev, P. S. S. R. Krishnan, A. Tselev, E. Strelkov, A. Borisevich, O. V. Varenyk, N. V. Morozovsky, P. Munroe, S. V. Kalinin and V. Nagarajan, *Phys. Rev. B*, 2014, **89**, 054102.

Contributions

N.V, P.M, N.D.B, and P.S.S R.K designed the experiments. P.S.S R.K, W.-I. L., and Y.-H. C were responsible for the preparation and characterization of the samples. P.S.S R.K, Q.M.R., N.D.B., and J.A.A performed the STEM-HAADF studies, the EELS measurements and interpreted the data. J.A.A. and D.M.K. carried out the first-principles calculations and interpreted the results. All authors contributed to the manuscript and the interpretation of the data.

Competing financial interests

The authors declare no competing financial interests.

Corresponding author

Correspondence to: Professor Nagarajan Valanoor, nagarajan@unsw.edu.au +61 (0)2 9385 4263

A combination of atom column-by-column scanning transmission electron microscopy and density functional theory shows how epitaxial strain systematically alters the local electronic structure in mixed phase bismuth ferrite thin films.